Mechanism and Application of the Super-Periodic Structural Resonance in Storage Rings

FANG Shou-Xian QIN Qing[1)]

(Institute of High Energy Physics, CAS, Beijing 100049, China)

Abstract The traditional stability diagram for lattice design described in the space of the gradients of a focusing and a defocusing magnet is extended to study more complicated cases, in which the basic cell included in the super-periodic structure has more than two gradients as variables. With the method developed here, it is easy to understand the mechanism and the physics hidden behind these structural resonances and the method can be used to guide the choice of the working points of a given lattice. Applications on the real machines are given as examples, with the simulation results on dynamic aperture.

Key words structural resonance stopband, super-period, storage ring, dynamic aperture

1 Introduction

In most synchrotrons, super-periodic-lattice structures are routinely applied to fulfill various purposes. People used to choose the working point of a lattice in the Q_x-Q_y tune diagram. In this case, however, the influence of the structural resonance stopbands caused by the super-periodic structures can be obscured. Though the traditional stability diagram, often adopted in the early 1960's, can give a clear picture of the structural resonance stopbands, it is limited only for the very simple case like FODO lattice, where $K_{\rm f}$ and $K_{\rm d}$ are two field gradients of focusing and defocusing lenses of the cell structure. Thus, one can study the structural resonance stopbands in the $K_{\rm f}$-$K_{\rm d}$ stability diagram. We assert that only when the stability diagram is presented in the $K_{\rm f}$-$K_{\rm d}$ space, and not in the more commonly used tune space, would the effect of the super-periodic structural resonances become clear visibly. With this method, it is easy to optimize the lattice design by finding the largest stable region in this diagram, and weaken the effect from these stopbands[1].

Along with the development of accelerator, some new complex lattice cells were invented in 1980's, such as the Chasman-Green structure[2], and the quasi-FODO cell used in the Beijing Electron Positron Collider (BEPC)[3]. In such kinds of basic cells, the number of focusing and defocusing magnets is greater than two, and so is the number of variables $K_{\rm f,i}$ and $K_{\rm d,i}$. It is then necessary to study the structural resonance stopbands in the multi-dimensional space of $K_{\rm f,i}$-$K_{\rm d,i}$.

In this paper, we will first analyze the formation and the features of structural resonance stopbands in Section 2. As a practical application in Section 3, the high brightness mode of the Hefei Light Source (HLS) in National Synchrotron Radiation Laboratory (NSRL), Hefei, China, is studied along with its normal operating mode. We find even in the case of multi-variables, one can still extend the traditional stability diagram by means of a 2-dimensional subspace composed of any two gradient variables $K_{\rm f,i}$ and $K_{\rm d,i}$. With the improved method given in this paper,

Received 7 February 2006, Revised 6 March 2006
1) E-mail: qinq@ihep.ac.cn

the optimal choice of working point can be made in principle. Meanwhile, we illustrate further the mechanism of the formation of resonance stopbands and the corresponding features in the case of complex lattice cell structures. Finally, some conclusions are given in Section 4.

2 Formation and features of structural resonance stopband

2.1 Review on the basic of structural resonance

For convenience to review the basics of the structural resonance, we first discuss the simplest case, in which there are N identical FD lattice cells in a ring (labeled as Structure $\mathscr{A}$). Here, F represents the focusing lens in horizontal but defocusing in vertical for particle motion and D the defocusing lens in horizontal and focusing in vertical with the same length as F. $K_{\rm f}$ and $K_{\rm d}$ are field gradients of F and D lenses. For easy calculation, we take each mid point of F as the starting point of every period cell of {1/2F, D, 1/2F}, and find μ_x and μ_y (horizontal and vertical phase advances) of this structure as functions of x and y (stand for $K_{\rm f}$ and $K_{\rm d}$, respectively). If one takes x and y as axes, it gives the well-known stability diagram or the so-called "Necktie" diagram[4].

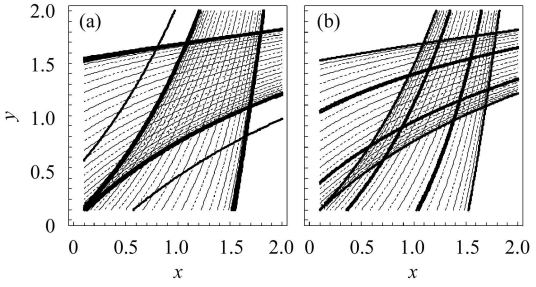

Fig. 1. Stability diagram of a typical structure. (a) Structure $\mathscr{A}$; (b) Structure $\mathscr{B}$.

To be specific, we consider the example in Fig. 1(a) with the number of period N=12, and the horizontal and vertical tunes of the particles are $Q_x = 12\mu_x/2\pi$ and $Q_y = 12\mu_y/2\pi$. There are 26 resonance lines of $Q_{x,y} = m/2$ (solid in Fig. 1(a)) with $\cos\mu_{x,y} = \cos m\pi/12$ (m=0, 1, 2, $\cdots$, 12), since the maximum phase advance in one cell is π and the maximum range of $Q_{x,y}$ is from 0 to 6. The 24 dashed lines in Fig. 1(a) refer to $\cos\mu_{x,y} = \cos(m\pi/12+\pi/24)$ (m=0, 1, 2, $\cdots$, 11), in which the crossing points are the centers of each stable block. The 4 deep black line bundles are the borders of the stable regions, corresponding to $\cos\mu_{x,y} = -1$ and 1.

2.2 Source of structural resonance stopbands

To find the source of structural resonance stopbands, we assume this pure periodic structure (N=12) as a virtual super-periodic structure of $N_{\rm S}$=4 with each super-period containing three identical cells of {1/2F, D, 1/2F}. Then, the stability diagram of such a virtual super-periodic structure (labeled as Structure $\mathscr{B}$) is shown in Fig. 1(b).

Figure 1(b) is very similar to Fig. 1(a), but the lines in Fig. 1(b) depict the values of $\cos\mu_{3x,y}$. Here, $\mu_{3x,y} = 3\mu_{x,y}$ with a variation range from 0 to 3π. Therefore, besides the four border lines of $\cos\mu_{3x,y} = \pm1$ (corresponds to $\mu_{3x,y}$=0 and 3π) in Fig. 1(b), there exists another set of four lines of $\cos\mu_{3x,y} = \pm1$, which corresponds to $\mu_{3x,y} = \pi$ and 2π, appearing inside the directions of x and y at the center of the "Necktie". To make this more visible, each line of $\cos\mu_{3x,y} = \pm1$ is shown with two additional lines of $\cos\mu_{3x,y} = \pm0.999$ in deep black, respectively. The whole stable region is divided into 9 blocks by these lines, with a block with apparent largest stable area appearing in the center of the stable "Necktie". It is important to point out that when the betatron tunes $Q_{x,y} = 4\mu_{3x,y}/2\pi$ satisfy $Q_{x,y} = 4m/2$ (m=0, 1, 2, and 3), the resonance lines appeared here are the real structural resonance lines of the super-periodic structure with the corresponding $\mu_{3x,y} = 0$, π, 2π, and 3π. These values of $\mu_{3x,y}$ are the base of the formation of the structural resonance lines. These lines are the base of the structural resonance stopbands and will become stopbands in a real super-periodic structure, as we will show later. Furthermore, the number of blocks of the divided stable region in both x and y directions equals to the number of the cells in each super-periodic structure, or the maximum phase advance of $\mu_{3x,y}/\pi$ in the super-periodic structure. All the other resonance lines of integers and half integers in Fig. 1(b) are non-structural resonance ones, corresponding to $\mu_{3x,y} = \pi Q_{x,y}/2$. The total number of

the stable regions is N_S^2. If N_S is an odd number, the second order resonance stopbands appear when $Q_{x,y}=N_S m/2$ (m=0, 1, 2, $\cdots$).

When a 1-meter straight section is inserted among every three cells in Structure $\mathscr{B}$, we will have a real super-periodic structure (labeled as Structure $\mathscr{C}$). Then, the stability diagram of this structure can be got with the same method as previous, shown in Fig. 2(a) as predicted above.

2.3 Complex lattice cell

A more realistic super-periodic structure is formed when we assume the gradient of one of the three D quadrupoles is $1.1y$ in the three cells of the above super-periodic structure (Structure $\mathscr{C}$), while the other F and D quadrupoles keep the same gradients of x or y (labeled as Structure $\mathscr{D}$). Thus, the multi-dimensional case with more than two variables can still be studied in a sub-space of 2-dimensional case with K_f and K_d as variables. Fig. 2(b) shows the stability diagram of this structure. Clearly, the structural resonance stopbands appear at the similar locations as Structures $\mathscr{B}$ and $\mathscr{C}$ with the values of $\mu_{3x,y}$ being ±1 too. The stable blocks which are close to the borders of stable region are squeezed by the structural resonance stopbands.

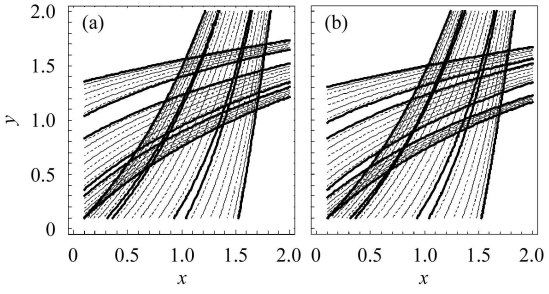

Fig. 2. Stability diagram of a super-periodic structure. (a) Structure $\mathscr{C}$; (b) Structure $\mathscr{D}$.

Clearly, it is very important to draw the stable diagram in an intuitionistic sub-space from the multi-dimensional case. Besides the method mentioned here, another one to deal with the problem is to let all the K_{fi} and K_{di} to be $xK_{fi,0}$ and $yK_{di,0}$, respectively, where $K_{fi,0}$ and $K_{di,0}$ are the strengths for quadrupoles in a given lattice, and x and y are the two variables of the 2-dimensional sub-space. Our calculations show that both of the two methods are very effective, and their results are very similar in the region near the nominal working point. The second method will be used in the applications of the real machines in Section 3. Up to now, we use a linear optics to get the stability diagrams and the structural resonance stopbands.

Now let's turn to the theoretical explanation of structural resonance stopbands. Consider two different periodic structures, say Pk and Pi, with Pk the main structure, which can be a periodic structure containing k identical cells or a quasi-periodic structure with k similar but not strictly identical cells. We assume the start or the end of this transfer matrix is the symmetric point of the periodic structure, so the transfer matrix of Pk is

$$M_k=\begin{pmatrix}\cos\mu_m & \beta_m\sin\mu_m\\ -\dfrac{1}{\beta_m}\sin\mu_m & \cos\mu_m\end{pmatrix}, \tag{1}$$

where μ_m, α_m, β_m and γ_m are Courant-Snyder parameters[5]. Let Pi be another lattice structure, with the transfer matrix

$$M_i=\begin{pmatrix}\cos\mu_1 & \beta_1\sin\mu_1\\ -\dfrac{1}{\beta_1}\sin\mu_1 & \cos\mu_1\end{pmatrix}. \tag{2}$$

If Pi has a symmetry around its center, we then divide Pi into two identical parts and put them at the two ends of Pk to form a periodic cell of {Pi/2, Pk, Pi/2}. The betatron phase advance μ in this structure and the β function of the starting point as follows can be expressed as:

$$\cos\mu=\cos(\mu_m+\mu_1)-\frac{(z-1)^2}{2z}\sin\mu_m\sin\mu_1, \tag{3}$$

$$\beta=-\frac{r_{12}}{\sqrt{1-\cos^2\mu}}, \tag{4}$$

and

$$r_{12}=\beta_1\left[\sin(\mu_m+\mu_1)-(z+1)\sin^2\left(\frac{\mu_1}{2}\right)\sin\mu_m+\left(\frac{1}{z}-1\right)\cos^2\left(\frac{\mu_1}{2}\right)\sin\mu_m\right]. \tag{5}$$

Here, $z=\beta_2/\beta_m$, β_2 is the envelope function at the central symmetric point of Pi alone. Unstable stopbands appear when $|\cos\mu|>1$. The number of stable blocks in one direction (x or y) equals to the maximum phase advance in the main structure in unit of π, i.e. μ_m/π. If the main structure consists of k

identical cells and the value of $\mu_{\rm m}$ has a range of $k\pi$, the number of the divided stable blocks per dimension will be k, which is independent on the number of super-periodic structure in the whole ring. It is worth pointing out that even the main structure is not necessarily a strictly periodic structure, but can be a quasi-periodic structure or very complex one without periodicity, if the total maximum phase advance is $k\pi$, the situation of the division of stable blocks still remains the same as above. In other words, no matter which quadrupole's strength changes in the main structure and how its parameters change, the structural resonance stopbands will appear, providing the value of $\mu_{\rm m}/\pi$ reaches a certain integer. This is the theoretical basis of the above method.

Figure 3 gives the contour lines of $\cos\mu$ in the plot of μ_1-$\mu_{\rm m}$ when k=8, among which the dark black and gray islands are unstable regions of $|\cos\mu|>1$. These islands are widest at $\mu_1=\pi/2$ and $3\pi/2$, but disappear near $\mu_1=\pi$ and 2π. This condition for disappearance of unstable islands corresponds to the case when Pi is an insertion of π phase advance, and belongs to the matched case. Another kind of matching happens when z=1, say $\beta_{\rm m}=\beta_2$. To a certain extent, the mismatching of the lattice can be regarded as a certain kind of magnet errors in the lattice. Of course this error or mismatching is considered to be sufficiently small.

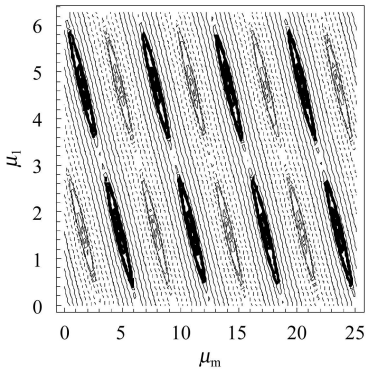

Fig. 3. Contour lines of $\cos\mu$.

2.4 Non-linear variation of β function near resonance stopbands

The variation of the β function can expose more features of structural resonance. We take the value of the β function at the starting point, say $\beta_{\rm in}$ given by Eq. (4), as an example to study its variation and let β_1=4m, z=0.7, and $\mu_{\rm m}$ varying from 0 to 2π, as shown in Fig. 4. The stable region is the narrowest when $\mu_1=\pi/2$ (dot-dashed lines), and the corresponding $\beta_{\rm in}$ varies most. We note that a condition when $\beta_{\rm in}$ becomes smaller should be avoided, since that necessarily implies the β somewhere in the periodic structure becomes larger. The closer to the region of $\mu_1=\pi$ or 0, the wider the stable region and the smaller the $\beta_{\rm in}$ varies, i.e., the closer the lattice structure approaches to the case of matching. In a fully matched case, we have $\beta_{\rm in}=\beta_1$. From Fig. 4, we can see that, around each stable region, the $\beta_{\rm in}$ at the right edge of the stable region increases quickly, while it approaches to 0 quickly too at the left edge. So the working point should be chosen in the smoothly changing part in the stable region, i.e., μ_1 should be made to stay far away from $\pi/2$. The variation of $\beta_{\rm in}$ as a function of $\mu_{\rm m}$ is periodic, but becomes very complicated and dependent on the lattice itself in the x-y plot without this kind of periodicity.

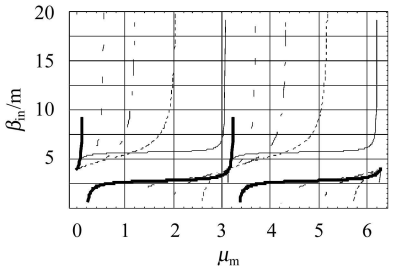

Fig. 4. Variation of $\beta_{\rm in}$ as a function of $\mu_{\rm m}$ when β_1=4m, z=0.7.
Lines represent $\mu_1=\pi/64$ (solid), $\pi/4$ (dashed), $\pi/2$ (dot-dashed), $3\pi/4$ (big-dashed) and 0.95π (thick and grey).

Some lattices unavoidably work near structural resonance stopbands, where β function locates in the area with asymmetrical change, we find the dynamic aperture will be asymmetric with respect to momentum deviation ($\Delta p/p$). The requirements of chromaticity correction are different for particles with $+\Delta p/p$ and $-\Delta p/p$. Clearly, how to find a lattice to have as small change of β function as possible is a problem worthy of further study.

3 Applications

As an example, we study the high brightness mode (HBM) and general purpose mode (GPM) of the HLS in NSRL, Hefei, China[1)], with the envelope and dispersion functions of a cell shown in Fig. 5. In these lattice configurations, the number of K's in a super-periodic structure is more than two. To review the chosen working points in our study, we can linearly change the gradients of all the focusing and defocusing quadrupoles in the super-periodic structure with a same scaling factor from their original values. By scaling all focusing quadrupoles with one factor x and all defocusing quadrupoles with another factor y, we can get a 2-dimensional x-y stability diagram to study the choice of working point, and give some guidance in principle.

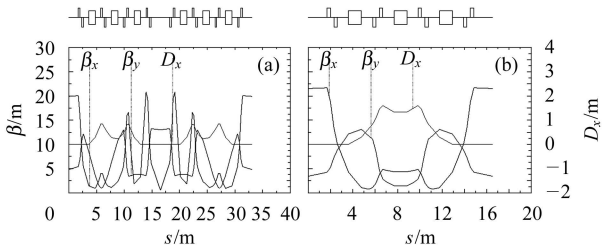

Fig. 5. Lattice configurations and twiss parameters of the HBM (a) and GPM (b) of HLS.

The super-periodic structure of the HBM is composed of two mirror-symmetrical structures, each with 8 quadruopoles. Q1 to Q8 correspond to the quadruoples from left to the midpoint shown in Fig. 5(a) and the 8 remaining quadrupoles from the midpoint to the right are mirror-symmetrical. The whole ring has a super-periodic structure with $N_{\rm S}$=2, and the tunes are Q_x/Q_y=5.82/2.42. The GPM structure has a simpler symmetry than that of the HBM, as shown in Fig. 5(b). Using the method mentioned above, we multiply all the gradients of F's with x, and all the gradients of D's with y. Fig. 6 shows the stability diagrams of the region near the chosen tunes.

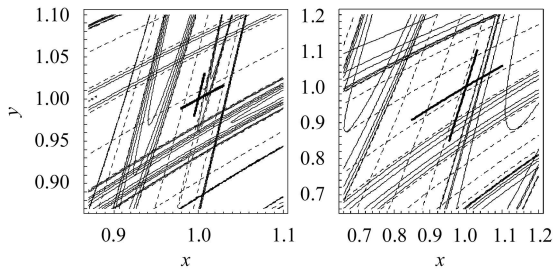

Fig. 6. Stability diagram near the working points of the HBM (left) and GPM (right) of HLS.

The U-shaped lines in Fig. 6 are due to the limited line number and CPU time. As to the HBM case, in Fig. 6(left), two structural resonance stopbands (solid lines) along the x axis (from left to right) correspond to Q_x=5 and 6. This is because the number of super-period $N_{\rm S}$=2, and thus all the resonance stopbands with Q's equal to integers become very wide. The crossing point of the two thick gray lines is the nominal working points, Q_x/Q_y=5.82/2.42. Although Q_y=2.42 is very close to a half integer, the corresponding resonance stopband is not a structural one, so it is not yet dangerous. But Q_x=5.82 is close to the integer structural resonance stopbands, affecting the performance of the machine. This is verified in Fig. 7, in which the β functions at the center of the long straight section vary with the scale factors x and y near this point. In Fig. 7, when x changes while keeping y=1, Q_x varies from 5 to 6 correspondingly and β_x increases when Q_x approaches 5 or 6, and is nearly a constant when Q_x is near 5.5. To the right side of the chosen working point (x and y=1), the β_x increases rapidly with x (from 22.4m to 41.5m in the range of Δx=0.004, $\Delta\beta/\Delta x = 4.8\times10^3$m), while to the left side, the β_x decreases not so rapidly. This difference causes difficulty of chromaticity correction, leading to an asymmetry of the dynamic aperture for the cases of $\pm\Delta p/p$. The performance of the actual machine can be seriously compromised. When y changes while keeping x=1, Q_y varies from 2 to 3 correspondingly, and β_y near the working point changes much less than β_x. This indicates the vertical oscillation of particles is more stable in this machine, and predicts that the vertical dynamic aperture should be

1) LI W M, ZHANG H. private communication, 2005.

larger than the horizontal one.

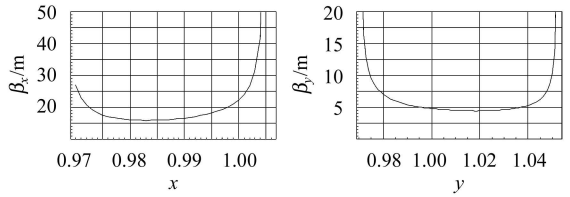

Fig. 7. β_x variation with x when y=1 (left) and β_y variation with y when x=1 (right) in HBM.

For the case of GPM, as shown in Fig. 6 (right), the crossing point of the two thick gray lines is the nominal working point Q_x/Q_y=3.58/2.58. Since the number of super-periods N_S=4, the structural resonance stopbands are somewhat sparse, and only appear when Q is an even integer. Four structural resonance stopbands (solid lines), each of which is consists of several solid lines, correspond to $Q_{x,y}$=2 and 4 and form 16 stable blocks (with the dashed lines as their borders) enclosed by the above solid lines' stopbands. It is fortunate that the horizontal tune Q_x=3.58 is not close to the structural resonance stopband Q_x=4, though the stable block where Q_x=3.58 is located is squeezed and becomes smaller in appearance. It is easy to find that the GPM has more and larger stable regions than the HBM, deducing that the GPM should have a better performance than the HBM.

Figure 8 shows how the β functions at the center of the long straight section of the GPM structure vary with x and y, respectively. Near the chosen working point, β_x changes from 21.5m to 23.5m in the range of Δx=0.005 ($\Delta\beta/\Delta x = 4\times10^2$m), which is an order lower than that in the HBM. The β_y only decreases 0.14m in the range of Δy=0.005. It is noticed that the horizontal axes span two integers, i.e., Q changes from 2 to 4. The β_y varies little when Q_y varies in the region 2.5, 3 and 3.5. Clearly, if the horizontal tune can be lowered somewhat, the GPM's performance should be greatly improved.

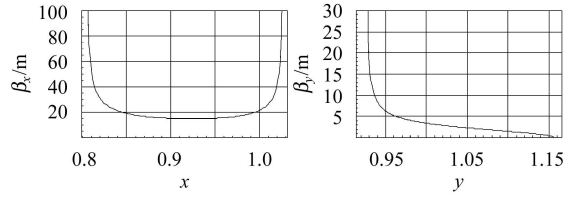

Fig. 8. β_x variation with x when y=1 (left) and β_y variation with y when x=1 (right).

To confirm the results, we investigate the detuning and the dynamic aperture of the GPM and HBM modes of the HLS. In the lattices of the GPM and HBM, 2 families of sextupoles are optimized for chromaticity correction. With these sextupoles, both the horizontal and vertical linear chromaticities of the GPM and HBM lattices are corrected to +1. Fig. 9 shows the tune variation of the two operation modes of the HLS versus the momentum deviation ($\Delta p/p$) of particles. It is easy to see that the tunes of the GPM lattice vary less and have smoother dependences, compared with the HBM lattice.

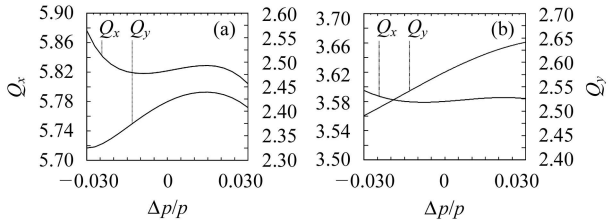

Fig. 9. Tune variation vs. momentum deviation for the operation modes of HLS. (a) HBM; (b) GPM.

The dynamic apertures, at the center of the long straight sections for the HBM and GPM lattices of the HLS are shown in Fig. 10. The code SAD[6] is used to calculate the dynamic apertures. No magnetic field errors are taken into account in the simulation. The vertical emittance is taken as half of the horizontal natural emittance, and the longitudinal oscillation is included during the 1024 turns of the tracking. One can see that the dynamic aperture of the GPM lattice is nearly three times larger than that of the HBM for both on- and off-momentum particles. The asymmetry of the dynamic aperture for particles with $\pm\Delta p/p$ is apparent in each mode, as expected from the previous analysis. Particles with positive momentum deviation have bigger dynamic apertures in both HBM and GPM. In the HBM, the vertical dynamic apertures are larger than the horizontal ones, which also confirm our previous deduction. This also coincides with the actual operating experience of the HLS. It's worth pointing out here that the dominant reason for the smaller dynamic aperture of the HBM is that working points are closer to the structural resonance stopbands than those of the GPM. Under this

circumstance, the sextupoles' strengths of the HBM are hard to be optimized to have a better dynamic aperture.

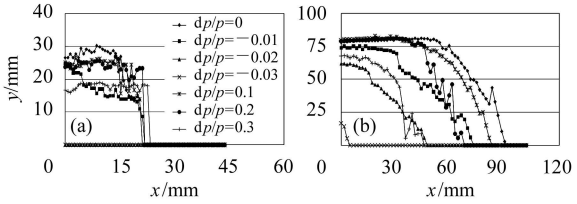

Fig. 10. Dynamic aperture of the two modes of the HLS lattice. (a) HBM; (b) GPM.

For comparison, we investigate the lattice of the BESSY- Ⅰ [7] in Germany. Fig. 11(a) shows the lattice configuration, and Twiss functions in a standard cell. The nominal working point is Q_x/Q_y=5.55/3.25, and the number of super-periods is $N_{\rm S}$=2. Note that the BESSY- Ⅰ lattice has one more quadrupole on the left side of the standard cell than that of the HLS.

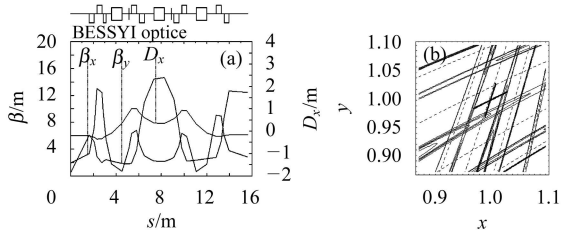

Fig. 11. Lattice configuration of the BESSY-Ⅰ and its twiss parameters in a standard cell (a) and the stability diagram near the nominal working points (b).

Figure 11(a) shows the stability diagram of the lattice of the BESSY- Ⅰ near its working point. The structural resonance stopbands (solid lines) in the figure correspond to Q_x=5 and 6, Q_y=3 and 4, respectively. Since the working point (crossing point of the two thick gray lines) is far away from these stopbands, the β functions at the center of the long straight section should be in a smooth region, as shown in Fig. 12. Additionally, the structural resonance stopbands in Fig. 11(b) are much narrower than those in Fig. 6(left), which means the corresponding driving harmonics of the lattice are relatively lower. We can see from the comparison that the performance of the HBM of the HLS could be improved if its horizontal tune Q_x is moved closer to 5.5.

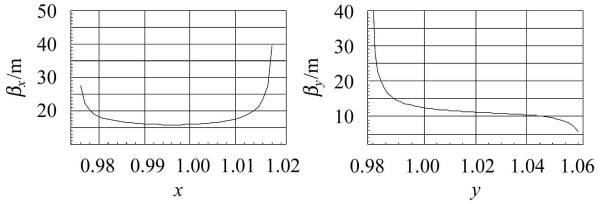

Fig. 12. β_x variation with x when y=1 (left) and β_y variation with y when x=1 (right).

It is necessary to point out that the method we applied above adopts the 2-dimensional sub-space in the multi-dimensional gradient variables. If we take any two of the gradients as variables and keep other parameters constant to construct a different 2-dimensional space, we can find that they will have the same characteristics. The reason is that the formation of the structural resonance stopbands comes from the harmonic number of the super-periodic resonance in the lattice configuration, and is not determined by how in detail the stopbands are approached by any of the two variables being varied. This has been demonstrated from the above discussions. No matter which two gradients in a super-periodic structure are being varied, the structural resonance stopbands will be generated as long as the absolute value of $\cos\mu_{3x,y}$ is bigger than 1.

4 Conclusions

The formation of the structural resonance stopbands and their features are described in this paper. With the new method developed here, the multi-dimensional case with more than two variables for a complex lattice can still be studied in a sub-space of 2-dimensional case with $K_{\rm f}$ and $K_{\rm d}$ as variables.

For a given super-periodic structure, the number of the divided stable blocks per dimension in the stability diagram is independent on the number of super-periodic structure in the whole ring. Even the main structure is not necessarily a strictly periodic structure, but can be a quasi-periodic or a very complex one without periodicity, the situation of the division of stable blocks still remains the same. The total number of the stable regions in the Necktie diagram has a tight relation with the maximum phase advance μ of the main lattice cell, but it is independent on

the number of super-period N_S. When μ/π equals to integer, the structural resonance stopbands appear. Using the method developed upon the above theory, we can study the stability diagram of a lattice with any complex cell as its main structure, giving a clear physics picture to choose working point.

Moreover, when the working point of a lattice approaches integer and half-integer structural resonance stopbands, the β function undergoes a dramatic nonlinear change. This change is the main source of the large reduction of dynamic aperture and the strong asymmetry with respect to the positive and negative momentum deviations observed in simulation codes.

To optimize the lattice design of a storage ring, therefore, we should pay more attention to the structural resonance stopbands caused by the superperiodic structure. We should not be content with using the Q_x-Q_y diagram to choose the working point, but should firstly refer to the stability diagram, which adopts focusing gradients as variables. Only in this stability diagram in quadrupole strengths can we be provided in general a clear picture of how to find quickly the preferred stable region and to locate the working point in the stable region. So when the working points of a lattice have to be close to an integer or half-integer, one should choose the region where the β function changes comparably smoothly. At last, the check with dynamic aperture simulation can help one to convince the lattice design and can further reveal the higher order resonance effect. This design principle has been applied to the practical cases, and the results from the operating lattices confirm all the conclusions we got.

We would like to thank Dr. H. Zhang and Prof. W.M. Li from NSRL, China, for useful discussions. Special thanks are given to Prof. A. Chao from SLAC, USA, for his help.

References

1 Holt J R, Newns H C. The A.G. Synchrotron with Superperoid Structure. Proc. of 1961 International Conference on High Energy Accelerator, 1961. 217
2 Chasman R, Green G K, Rowe E M. IEEE Trans. Nucl. Sci., 1975, **NS-22**: 1765
3 FANG S X et al. HEP & NP, 1986, **10**: 207(in Chinese) (方守贤等. 高能物理与核物理, 1986, **10**: 207)
4 Bryant P J, Johnsen K. The Principles of Circular Accelerators and Storage Rings. Cambridge: Cambridge University Press, 1993. 38
5 Courant E D, Synder H. Ann. Phys., 1958, **3**: 1
6 SAD Code Homepage. http://acc-physics.kek.jp/SAD/sad.html
7 Murphy J. Synchrotron Light Source Data Book. (Version 4). 1996. BNL-42333

储存环超周期结构共振带的形成机制及应用

方守贤　秦庆[1)]

(中国科学院高能物理研究所　北京　100049)

摘要　将环形加速器磁聚焦结构设计中, 传统的聚焦和散焦磁铁强度空间中的稳定图方法, 应用到更复杂的含有两个以上磁场梯度变量的超周期结构中, 从而更深入地理解结构共振的形成机制和隐含的物理意义. 利用文中给出的方法, 可以指导环形加速器磁聚焦结构的工作点选择. 对于一个给定的磁聚焦结构, 由于结构共振而导致的束流包络函数变化的不对称性, 则是其动力学孔径不对称的一个重要原因. 作为实例, 给出了在实际机器上的具体应用, 同时给出了动力学孔径的模拟计算结果.

关键词　结构共振带　超周期　储存环　动力学孔径

2006 – 02 – 07 收稿,　2006 – 03 – 06 收修改稿

1) E-mail: qinq@ihep.ac.cn